Energy Storage Materials 24 (2020) 129–137

Contents lists available at ScienceDirect

Energy Storage Materials

journal homepage: www.elsevier.com/locate/ensm

Flexible lignin carbon membranes with surface ozonolysis to host lean lithium metal anodes for nickel-rich layered oxide batteries

Lei Tao [a,b,c], Zhengrui Xu [b], Chunguang Kuai [b,d], Xuerong Zheng [b,d], Candace E. Wall [b], Chao Jiang [a], Alan R. Esker [b], Zhifeng Zheng [a,**], Feng Lin [b,*]

[a] Fujian Engineering and Research Center of Clean and High-valued Technologies for Biomass, College of Energy, Xiamen University, Xiamen, 361102, PR China
[b] Department of Chemistry, Virginia Tech, Blacksburg, VA, 24061, USA
[c] College of Materials Science and Engineering, Northeast Forestry University, Harbin, 150040, PR China
[d] College of Materials Science and Engineering, Tianjin University, Tianjin, 300072, PR China

ARTICLE INFO

Keywords:
Lignin
Nickel rich
Surface ozonolysis
Carbon membrane
Lithium metal battery

ABSTRACT

The implementation of the high-capacity Li metal anode in practical batteries has not been successful due to the short lifespan and severe safety concerns resulting primarily from low Coulombic efficiency and Li dendritic growth. Lightweight carbon skeletons are considered promising for hosting the lithium metal anode to overcome these limitations. Furthermore, the lithium metal loading must be minimized from the cost and safety standpoint, leading to the need of developing long cycle life "lean Li metal anodes". Herein, we report a surface ozonolysis approach to homogenize Li nucleation sites and to guide the uniform Li metal deposition on flexible oxygen-enriched lignin-derived carbon membranes (OLCMs). The resulting lean OLCM@Li composite anode allows for stable Coulombic efficiency (>98% over 230 cycles), long cycle life (>1, 000 h), and small voltage hysteresis (<20 mV) in OLCM@Li||Li cells. When assembled in nickel-rich layered oxide batteries with the $LiNi_{0.8}Co_{0.1}Mn_{0.1}O_2$ cathode, the lean OLCM@Li composite anode enables highly reversible capacity, high Li utilization, and improved cell cycle life. Therefore, the low-cost and mild surface ozonolysis processed lignin-based carbon membranes represent a promising class of materials for stabilizing lean Li metal anodes.

1. Introduction

With the rapid development of advanced portable electronics devices, and electric vehicles, conventional graphite anodes, with a low theoretical capacity (372 mA h g^{-1}), cannot meet the demand of high-energy-density batteries [1,2]. In contrast, metallic Li has a high theoretical capacity of 3860 mA h g^{-1}, a low negative electrochemical potential of −3.04 V vs SHE, and low mass density of 0.534 g cm^{-3}, which make Li metal an attractive anode of choice for advanced Li metal batteries [3], such as lithium/sulfur [4], lithium/nickel-rich layered oxide [5], and lithium/oxygen batteries [6]. However, Li metal anode encounters several major challenges, including Li dendritic growth, and infinite volume changes during Li plating/stripping [7]. Consequently, these challenges lead to unstable solid electrolyte interphase (SEI) formation, low and rapidly decreasing Coulombic efficiency, poor lifespan, and even severe safety hazards [8]. Extensive works have been made to effectively relieve the Li dendritic growth by i) constructing strengthened SEI films through optimizing the electrolyte composition [9–12], ii) employing solid electrolytes [13,14], and iii) engineering artificial SEIs [15,16]. Furthermore, many studies have focused on designing conductive porous current collectors to accommodate the infinite volume changes of Li metal, such as three-dimensional (3D) metal skeletons [17–21]. However, the high density associated with the metal skeletons drastically decreases the overall specific energy density of the electrode [22,23]. Featured by the light-weight properties, 3D porous carbon materials are superior to 3D metal skeletons for hosting Li metal [24–30]. However, without proper surface functionalization, the neat carbon surfaces are typically lithiophobic, resulting in uneven Li deposition (e.g., lithium metal clustering), and potentially Li dendritic growth during battery cycling [27–31]. The fundamental chemistry shows that the affinity of Li with a nonmetal element is dependent on the electronegativity difference (the polarity of the Li-nonmetal bond) [32]. A more polar bonding may lead to a favorable and stronger Li-nonmetal interaction. Recent theoretical calculations and experiments have also demonstrated this basic

* Corresponding author.
** Corresponding author.
E-mail addresses: zhifeng.zheng@xmu.edu.cn (Z. Zheng), fenglin@vt.edu (F. Lin).

https://doi.org/10.1016/j.ensm.2019.08.027
Received 26 July 2019; Received in revised form 23 August 2019; Accepted 29 August 2019
Available online 31 August 2019

principle that nitrogen-containing, oxygen-containing functional groups and transition metal-containing allow for stronger binding energy toward Li metal, which can render a lower Li nucleation barrier and, thus, a smaller nucleation overpotential [25,33–36]. Evenly distributed functional groups at the surface of a carbon skeleton should homogenize the lithiophilicity across the skeleton and enable homogenous Li nucleation [37–39]. This was experimentally demonstrated in recent studies [33,34,37–41]. To date, most surface-functionalized carbon materials are obtained from precursors that inherently contain nitrogen and oxygen or through aggressive processing methods such as strong acid [33], ammonia [25,39,40] or oxygen activation processes [42]. Therefore, it is imperative to develop an efficient, quantifiable, low-temperature, and mild method to generate functional groups on carbon skeletons.

The full-cell investigation of coupling a lean Li metal anode with a practical high energy cathode will provide insights into understanding the Li electrochemical properties, which is not readily available in Li||Li symmetric cells. Nickel-rich layered oxides, such as $LiNi_{0.8}Co_{0.1}Mn_{0.1}O_2$ (NMC811), represent a family of prominent cathode materials with potential to improve energy densities, reduce cost and enhance safety of batteries [43–49]. When paired with a lean Li metal anode, the nickel-rich layered oxide battery can potentially push the cell specific energy to above 350 Wh/kg [1]. Therefore, understanding how a nickel-rich layered oxide battery perform with a lean Li metal anode will provide a knowledge base for developing practical Li metal nickel-rich layered oxide batteries.

In this study, we present lightweight, low-cost, flexible, and natural lignin-derived carbon membranes that are surface oxygenated through an ozonolysis technique. The resulting oxygen-enriched carbon membranes not only guide the homogeneous Li metal nucleation and growth with an ultra-small nucleation overpotential [25,33,50] but also enable stable Coulombic efficiency, long cycle life, small voltage hysteresis, and high critical current density. The OLCM@Li||NMC811 cells deliver comparable capacity to the bulk Li||NMC811 cells. Furthermore, because of the decelerated lithium consumption in the OLCM@Li anode, these cells exhibited much longer cycle life than the ones assembled with the Cu@Li or LCM@Li anodes. The surface ozonolysis increases the capability of carbon materials to accommodate and retain Li metal for high energy nickel-rich layered oxide batteries. The OLCM can host Li metal with tunable areal capacity, thus future work should focus on further optimizing the anode/cathode capacity ratio.

2. Results and discussion

As shown in Fig. 1a, natural lignin was reacted with phenol/

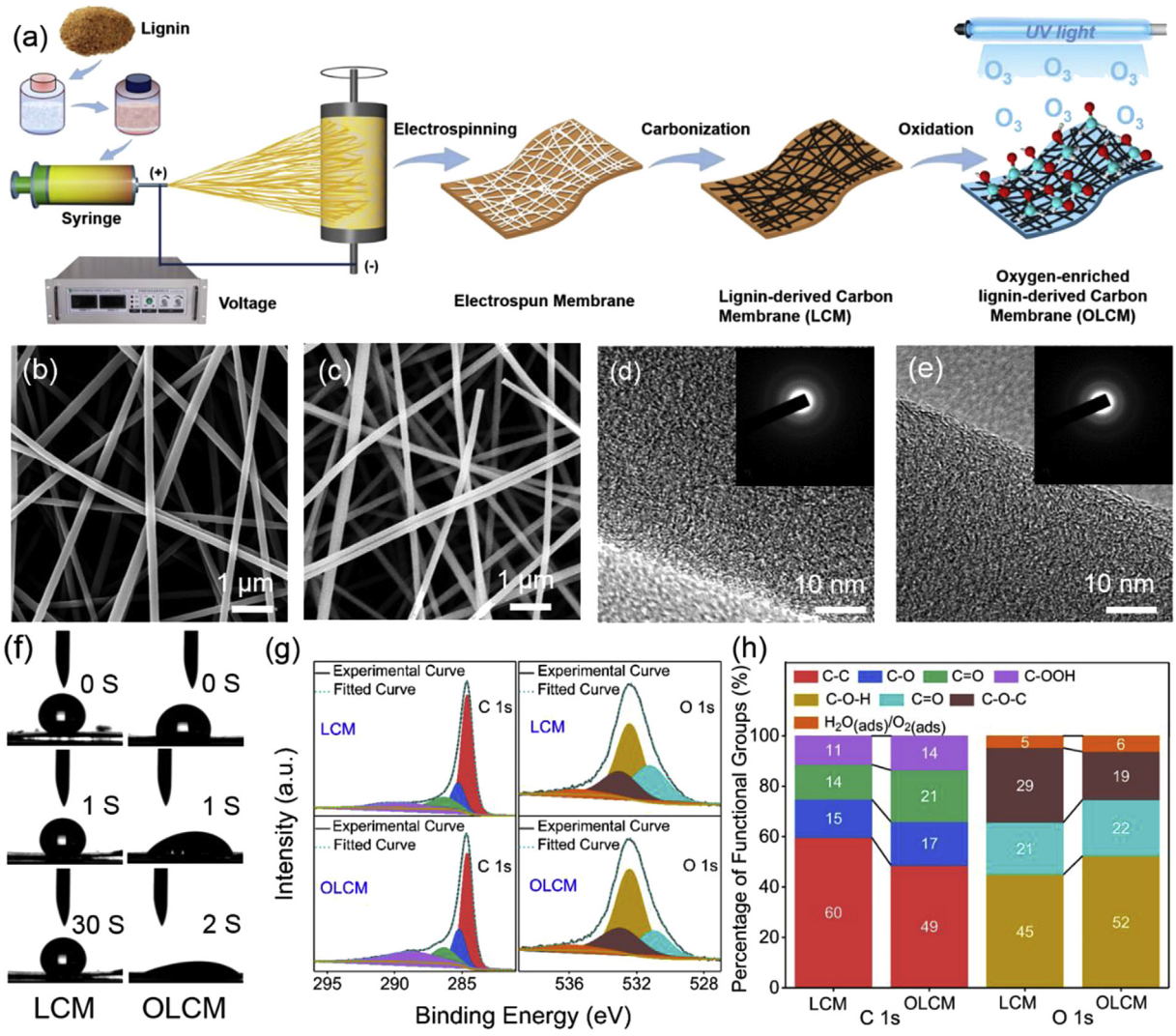

Fig. 1. (a) Schematic diagram of the fabrication process of the LCM and OLCM. (b), (c) Representative SEM images of the LCM and OLCM, respectively. (d), (e) TEM images of LCM and OLCM, respectively. Insets: selected area electron diffraction (SAED). (f) Water contact angle images of the LCM and OLCM. (g) XPS C 1s and O1s spectra of the LCM and OLCM. (h) Quantification of the functional groups present on the surfaces of LCM and OLCM. The same color codes apply to (g) and (h). (For interpretation of the references to color in this figure legend, the reader is referred to the Web version of this article.)

formaldehyde resin to afford the main component of the electrospinning solution. Subsequently, the electrospinning solution was ejected onto the roller to generate a nanofiber membrane. The nanofiber membrane was then peeled off from the aluminum foil and dried at room temperature (Fig. S1a, Supporting Information). The dried membrane was then carbonized to obtain the lignin-based carbon membrane (LCM) (Fig. S1b, Supporting Information). The specific surface area of the LCM was 424 $m^2 g^{-1}$, with a mean pore diameter of 0.9 nm (Fig. S2, Supporting Information). To prepare the OLCM, the carbonized LCM was subjected to the UV/O_3 treatment for 2 h, O_3 oxidizes the LCM and facilitates the generation of oxygen-containing functional groups on the surface (i.e., surface ozonolysis). After the ozonolysis, the carbonized membrane was still highly flexible and retained the pristine shape without noticeable damage after repeated folding and unfolding (Movie S1, Supporting Information). The LCM and OLCM were woven from numerous intertwined bead-free nanofibers with smooth surfaces and uniform diameters of ~200 nm (Fig. 1b and c) and a thickness of ~76 μm (Fig. S3, Supporting information). These materials were highly amorphous, as shown by the high-resolution transmission electron microscopy (HRTEM) images and the corresponding selected area electron diffraction (SAED) (Fig. 1d and e). Two characteristic carbon Raman bands at 1340 cm^{-1} and 1585 cm^{-1} are ascribed to the disordered sp^3 carbon (D band) and the ordered sp^2 carbon (G band), respectively (Fig. S4, Supporting Information). The intensity ratio between the D and G bands showed negligible changes after the ozonolysis. All these results confirmed that the ozonolysis is a mild method that specifically modulates the surface properties without disrupting the bulk properties of the LCM. Therefore, our materials provide a good platform to precisely investigate the impact of the carbon surface chemistry on the cycle life of lean lithium metal anodes.

Supplementary video related to this article can be found at https://doi.org/10.1016/j.ensm.2019.08.027.

The survey XPS spectra showed that the LCM and OLCM mainly contained C and O elements. Obviously, the oxygen content increased significantly from 2.9% to 12.5% after the surface ozonolysis (Fig. S5, Supporting Information). The C 1s spectra were deconvoluted into C–C (284.6 eV), C–O (285.2 eV), C═O (286.3 eV) and C–OOH (289.7 eV) (Fig. 1g) [51]. The O 1s spectra were deconvoluted into C═O (531.2 eV), C–O–H (532.4 eV), C–O–C (533.1 eV) and H_2O or O_2 (chemisorbed oxygen, 535.6 eV) (Fig. 1g) [51]. These results showed that the OLCM surface was populated with much more oxygen-containing functional groups than the LCM surface (Fig. 1h). The contact angle measurements further confirmed that the oxygen-containing functional groups were stably created on the surface of OLCM (Fig. 1f). The LCM exhibited a hydrophobic surface with the capability of resisting DI water penetration

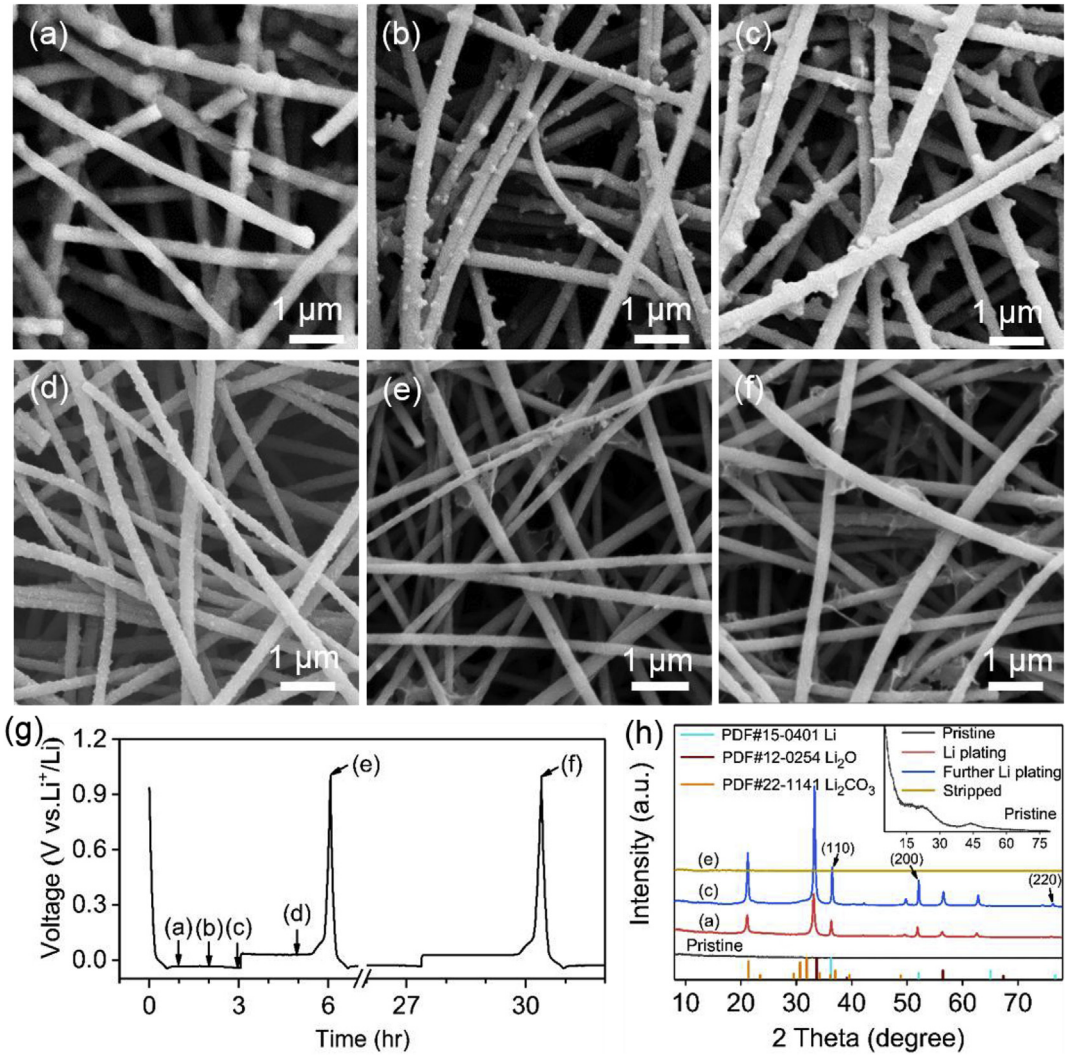

Fig. 2. SEM images of the OLCM at different stage of Li plating measured at 1 mA cm^{-2} for (a) 1 mA h cm^{-2}, (b) 2 mA h cm^{-2}, (c) 3 mA h cm^{-2}. And at different stage of Li stripping measured at 1 mA cm^{-2} for (d) 2 mA h cm^{-2}, (e) 3 mA h cm^{-2}, (f) after the 5th stripping for 3 mA h cm^{-2}. (g) The Li plating/stripping states (a–f) are indicated in the galvanostatic discharge/charge voltage profile at 1 mA cm^{-2} for 3 mA h cm^{-2}. (h) High resolution synchrotron X-ray diffraction (XRD) patterns for the OLCM prior to (Pristine) and after different "Li plating/stripping states": the (a), (c), and (e) correspond to the SEM images with the same letters.

for over 30 s. OLCM presented a hydrophilic surface and absorbed DI water within 2 s. There have been studies showing that lithiophilicity increases with increasing surface oxygenated groups [33,40], and hydrophilicity also increases with increasing surface oxygenated groups [52]. Therefore, empirically, hydrophilicity may be a good approximation for lithiophilicity. Thus, the oxygen-containing functional groups would be beneficial for facilitating the uniform Li nucleation and growth. Compared to conventional strong acid treatments that are typically tedious and detrimental to the morphological and bulk properties of carbon skeletons, the ozonolysis is a robust, mild, facile and low-cost alternative to obtain oxygen-containing functional groups. Such a surface-targeted processing technique allows for investigating the interaction between Li metal and the carbon surface without altering the morphological or bulk properties.

The Li deposition process on the LCM and OLCM materials was investigated in details. A constant 1 mA cm^{-2} current density was used on the LCM and OLCM electrodes and the change of potential vs. time was recorded (Fig. 2g and Fig. S6, Supporting Information). Fig. 2a–c shows the morphological evolution (top view) of the OLCM with the increase Li metal loading during the plating process. Li nanoparticles got gradually plated on the fiber, and no visible micron-sized Li agglomerate was detected on the OLCM at a 1 mA h cm^{-2} loading (Fig. 2a). This result indicates that a high concentration of oxygen-containing functional groups provided high-density Li nucleation sites that allow for highly dispersed Li nanoparticles on the OLCM skeleton. When the Li loading was increased to 2 mA h cm^{-2}, abundant Li nanoparticles could be immobilized on the nanofiber with a slight increase in size (Fig. 2b). This phenomenon was more evident as the Li loading reached 3 mA h cm^{-2} (Fig. 2c). Similar results were found in the cross-section SEM image of the OLCM (Fig. S7, Supporting Information). The Li nanoparticles was initially deposited on the carbon skeleton, and then further formed a Li metal layer wrapping around the carbon skeleton, and ultimately completely enveloped the carbon skeleton. As Li plating was further increased to 6 mA h cm^{-2}, a fully covered flake-like Li was observed on the skeleton of the nanofibers (Fig. S8, Supporting Information). A large loading of Li nanoparticles could be uniformly deposited onto carbon skeleton, demonstrating the desirable structural characteristics of the OLCM as a Li metal host. Such a favorable Li deposition is absent from the LCM (Figs. S9a–9c, Supporting Information). For the LCM, agglomerated Li metal particles were found in the stage of the early plating process. With more Li plating, the micron-sized Li particles started to agglomerate, and ultimately led to uneven pancake-like Li pieces with rough surfaces. The nanofiber surface or skeleton remained relatively smooth after Li plating, indicating that Li metal could barely nucleate on the LCM surface. Indeed, the cross-sectional SEM (Figs. S9d–9f, Supporting Information) confirmed almost no Li particles formed on the LCM carbon skeleton, even at higher levels of Li deposition. Furthermore, there were a noticeable number of agglomerates on the LCM after full stripping (Figs. S9g–9h, Supporting Information). For previously reported electrochemical Li deposition in 3D porous carbon materials, dense and uniformly distributed Li nucleation sites were hardly observed at the initial stage [27–29,53]. Here oxygen-containing functional groups on the OLCM guided the Li nucleus to uniformly disperse on the fiber skeleton with a lower overpotential (discussed later). Furthermore, the high specific surface area of the OLCM reduced the area-specific current density, which might help regulate the Li nucleation and growth.

The deposited Li could be reversibly stripped from the OLCM without interrupting the structural integrity of the OLCM. Fig. 2d and e shows that the deposited Li metal was gradually removed from the OLCM skeleton without interfering the 3D architecture after a whole stripping process finished at 1.0 V. When the deposited Li was stripped for 2 h (Fig. 2d), the observed density and size of the Li nanoparticles significantly decreased on the OLCM skeleton. Eventually, with the whole stripping process was completed (deposited Li was stripped for 3 h), the OLCM returned to its initial morphology and retained the excellent structural integrity due to its superior flexibility. After 5 cycles of the above plating/stripping process, the OLCM still maintained intact structure without the presence of Li particle agglomerates, Li dendrites, or "dead" Li (Fig. 2f), suggesting that the Li dendrite can be effectively inhibited during the plating/stripping process. This was confirmed by high resolution synchrotron X-ray diffraction (XRD) (Fig. 2h). With 1 mA h cm^{-2} Li deposition, three characteristic peaks at 36.4°, 52.0°, and 76.3° corresponding to the (110), (200), and (220) plane of the metallic Li were observed on the pristine OLCM. Further increasing the plating to 3 mA h cm^{-2}, the intensity of the Li metal peaks increased. After completely stripped, the characteristic Li peaks vanished, indicating that Li was reversibly stripped from the OLCM. The unidentified peaks were presumably from the crystalline products of the Li-electrolyte reaction that were also reversibly eliminated during stripping. Therefore, the actual metallic Li on the carbon skeleton was much leaner than the nominal loading calculated from the coulometry. TEM was performed to further reveal the distinct plating behavior of the OLCM relative to that of the LCM (Fig. S10, Supporting Information). For the LCM, large particles were randomly formed on the nanofibers, indicating an uneven Li plating behavior (Figs. S10a–10c, Supporting Information). For the OLCM, uniform nanoparticles were formed on the OLCM skeleton (Figs. S10d–10f, Supporting Information), indicating that oxygen-containing functional groups contributed positively to the homogeneous Li plating on the OLCM.

Overpotential is a crucial parameter to determine the affinity of Li nucleus to the scaffold. The smaller the absolute value of the overpotential, the better the affinity and more conducive to uniform Li nucleation. Mass transfer overpotential is considered as one type of the overpotential, which is mainly depends on the current density and the migration properties of the Li ions in the electrolyte [25]. Fig. 3a shows the Li plating/stripping profiles of the OLCM measured at various currents of 0.5–5.0 mA cm^{-2} with same Li capacity of 2.0 mA h cm^{-2}. All the plating/stripping profiles demonstrated flat voltage plateaus with small mass transfer overpotentials. For the current densities of 0.5, 1.0, 2.0, 3.0, 4.0, and 5.0 mA cm^{-2}, the mass transfer overpotentials were 19, 31, 38, 48, 67, and 87 mV, respectively (***inset of*** Fig. 3a). The OLCM can still maintain a small mass transfer overpotential even at a high current density, revealing the rapid Li cation migration kinetics in electrolyte and superior interfacial properties. The nucleation overpotential another type of overpotential, which mainly depends on the lithiophilicity of the electrode surface [37]. Fig. 3b compares the initial voltage profiles of three electrodes at current density of 1 mA cm^{-2} with same capacity of 3 mA h cm^{-2}. The initial Li nucleation on the LCM electrode and the planar Cu required large nucleation overpotentials of 34 and 58 mV, respectively, whereas the OLCM electrode demonstrated a remarkably lower overpotential of 19 mV, which was likely associated with the oxygen-containing functional groups on the OLCM [33]. A lower initial nucleation overpotential allowed for populated and homogeneously distributed nucleation sites and thus uniform Li deposition, which was consistent with the deposition behavior (Fig. 2a). To further validate this hypothesis, the Coulombic efficiency (CE) of three electrodes were investigated. Fig. 3c and d shows that at Li plating capacity of 1 mA h cm^{-2}, the Cu showed a fast decay in CE to <90% after 60 cycles at 1 mA cm^{-2} and <90% after 55 cycles at 3 mA cm^{-2}, signifying the electrode failure due to the formation of "dead" Li [28,29]. The LCM showed better cycling performance than the planar Cu. The cycling was stable at above 90% CE for 140 cycles at 1 mA cm^{-2} and above 90% CE for 77 cycles at 3 mA cm^{-2}. In sharp contrast, the OLCM exhibited improved cycling performance, maintaining >98% CE over 230 cycles at 1 mA cm^{-2} and >98% CE over 135 cycles at 3 mA cm^{-2}. When increasing the Li capacity to 3 mA h cm^{-2}, the CE of the OLCM maintained above 90% for 80 cycles at 1 mA cm^{-2} (Fig. 3e). In contrast, the CE of the LCM decayed rapidly to 55% after only 21 cycles and demonstrated obvious fluctuations, and the cell containing the Cu electrode shorted after only 16 cycles. Impressively, the OLCM can still maintain a high CE above 90% for 40 cycles after further increasing the plating to 6 mA h cm^{-2}, whereas the CE of the LCM electrode declined rapidly after only 10 cycles

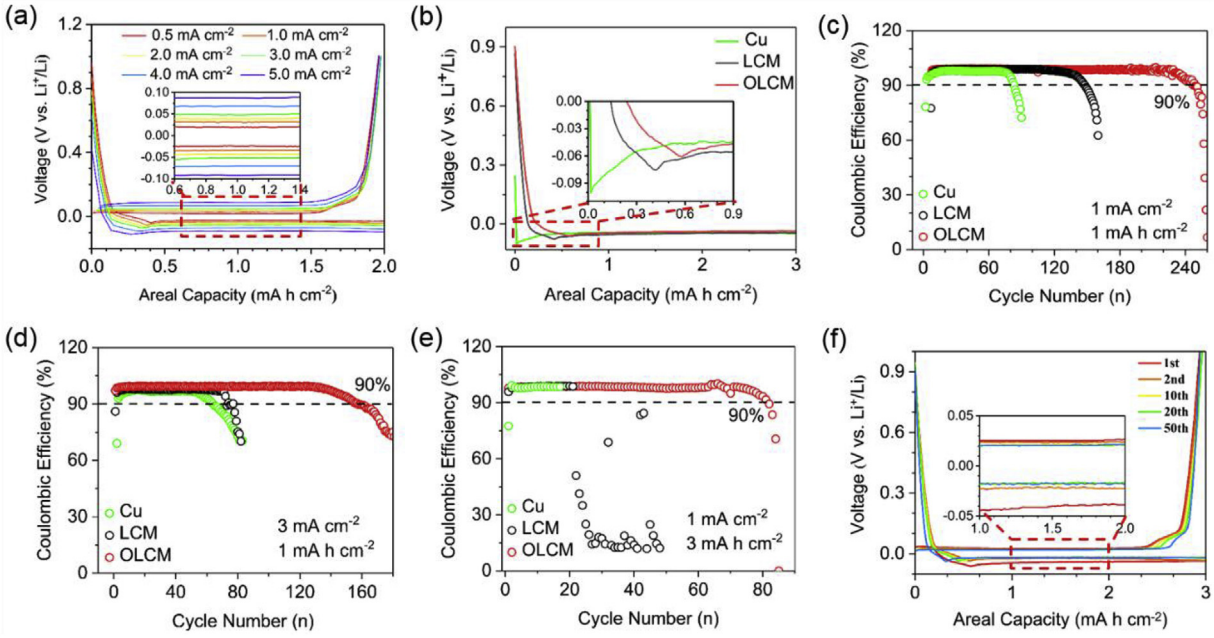

Fig. 3. (a) Voltage profiles of Li plating/stripping on OLCM measured at various current densities of 0.5, 1.0, 2.0, 3.0, 4.0 and 5.0 mA cm^{-2} with Li capacity of 2 mA h cm^{-2}. (b) Initial Li nucleation overpotential of planar Cu, LCM and OLCM. Coulombic efficiency evaluation on the planar Cu, LCM and OLCM measured at (c) 1 mA cm^{-2} for 1 mA h cm^{-2}, (d) 3 mA cm^{-2} for 1 mA h cm^{-2}, and (e) 1 mA cm^{-2} for 3 mA h cm^{-2}. (f) Voltage profiles of the Li plating/stripping process on the OLCM electrode at 1 mA cm^{-2} for 3 mA h cm^{-2}.

(Fig. S11a, Supporting Information). The plating/stripping profiles of the Li capacities of 3 and 6 mA h cm^{-2} at the same current density of 1 mA cm^{-2} were shown in Fig. 3e and Fig. S11b, respectively. Both area capacities exhibited the stable plating/stripping behavior with small voltage hysteresis.

To further evaluate the long cycle performance of these composite electrodes, we fabricated four cells (Cu@Li||Li foil, LCM@Li||Li foil, OLCM@Li||Li foil, and Li foil ||Li foil) to investigate voltage fluctuations the during battery cycling. Fig. 4a shows the Li metal plating/stripping profiles of these cells measured at same current density of 1 mA h cm^{-2} with same Li capacity of 1 mA h cm^{-2}. Remarkably, the OLCM@Li||Li foil cell demonstrated a minimal voltage hysteresis and manifested a long cycle life of 1000 h with flat voltage profiles and stable overpotential. This result is consistent with the CE results (Fig. 3c). For the LCM@Li anode, the voltage increased noticeably after 450 h of Li plating/stripping, revealing the heterogeneous Li distribution at the nanofiber surface [41]. The Cu@Li anode showed a highly unstable voltage profile with larger overpotentials. This probably due to the unstable SEI layer resulting from continues fracture/growth of Li dendrites [23]. The symmetric Li foil||Li foil cell displayed relatively small voltage fluctuations, but the signs of the short circuit was observed after 240 h, earlier than the OLCM@Li||Li foil cell (Fig. 4a). In order to investigate the voltage fluctuation, the plating/stripping profiles of the 1st, 200th, and 400th cycles were magnified (illustration in Fig. 4a). Apparently, the OLCM@Li anode showed flat plating/stripping curves with much lower overpotentials than the LCM@Li, Cu@Li, and Li foil anodes. Even with increasing the current density to 3.0 mA cm^{-2} (Fig. S12, Supporting Information), the OLCM@Li anode still exhibited a small overpotential of 40 mV for over 170 h (255 cycles). However, the LCM@Li anode exhibited gradually increasing overpotential upon cycling and the cell was shorted after only 50 h, indicating the formation of Li dendrites. In comparison, the Cu@Li and Li foil anodes performed worse with wide range of voltage fluctuations and much higher overpotentials in the early cycles. The rate capability of the OLCM@Li and LCM@Li anodes were also performed by cycling cells at various current densities from 0.5 to 5.0 mA cm^{-2} for 1.0 mA h cm^{-2} (Fig. 4c). Importantly, the voltage hysteresis of the OLCM@Li anode remained steady at each respective current density and even at 5 mA cm^{-2}. Such stable performance was not available for the LCM@Li anode due to the Li dendrites grow easily at the high current densities, as shown in Fig. 4c. Such high-level electrochemical performance is impressive, especially in comparison with the recently reported carbon-derived skeletons (a comprehensive comparison is shown in Table S1, Supporting Information).

We then explored the application of the OLCM@Li anode for nickel-rich layered oxide batteries and studied the impact of Li utilization and consumption on the battery performance. We assembled nickel-rich layered oxide cells using $LiNi_{0.8}Mn_{0.1}Co_{0.1}O_2$ (NMC811) as the cathode with three different cathode/anode capacity ratios ($C_{NMC811}/C_{Li} = 1.6/6.0$, $C_{NMC811}/C_{Li} = 1.6/3.0$, and $C_{NMC811}/C_{Li} = 0.8/6.0$). Note that the actual metallic lithium on the carbon skeleton was much leaner than the nominal loading calculated from the coulometry here because some deposited Li would react with the electrolyte to form non-metallic Li compounds (Fig. 2h). It is also important to note that we cycled each battery to the cycle number where the rapid capacity fading took place. This way of presenting the data allowed us to not only understand how lithium consumption happened but also to investigate the carbon surface chemistry-lithium consumption relationship in a lean lithium metal anode system [54]. Figs. S13a and 13b show the typical galvanostatic charge-discharge voltage profiles of the nickel-rich layered oxide cells at 1.0C between 2.5 V and 4.5 V, and the corresponding discharge capacity and Coulombic efficiency were shown in Fig. 4d–e. It is noteworthy that the OLCM, without Li metal loading, didn't provide any capacity in the OLCM||NMC811 cell (Fig. S13d, Supporting Information). The capacity increase during the initial cycles could be attributed to the activation process of the NMC811 cathode used (electrolyte wetting of the porous electrode) [55]. The discharge capacity of LCM@Li and Cu@Li cells ($C_{NMC811}/C_{Li} = 1.6/6.0$) experienced a rapid decline after 55 cycles and 49 cycles, respectively (Fig. 4d). This phenomenon was reported previously and attributed to the continuous Li consumption during battery cycling [54], indicating the low Li utilization of the LCM@Li and Cu@Li anodes. In comparison, the OLCM@Li cell ($C_{NMC811}/C_{Li} = 1.6/6.0$) exhibited much better stability and delivered a reversible discharge capacity of 186 mA h g^{-1} at 1.0 C, and remained 157 mA h g^{-1} after 135 cycles (Fig. 4d), indicating the high Li utilization and decelerated Li

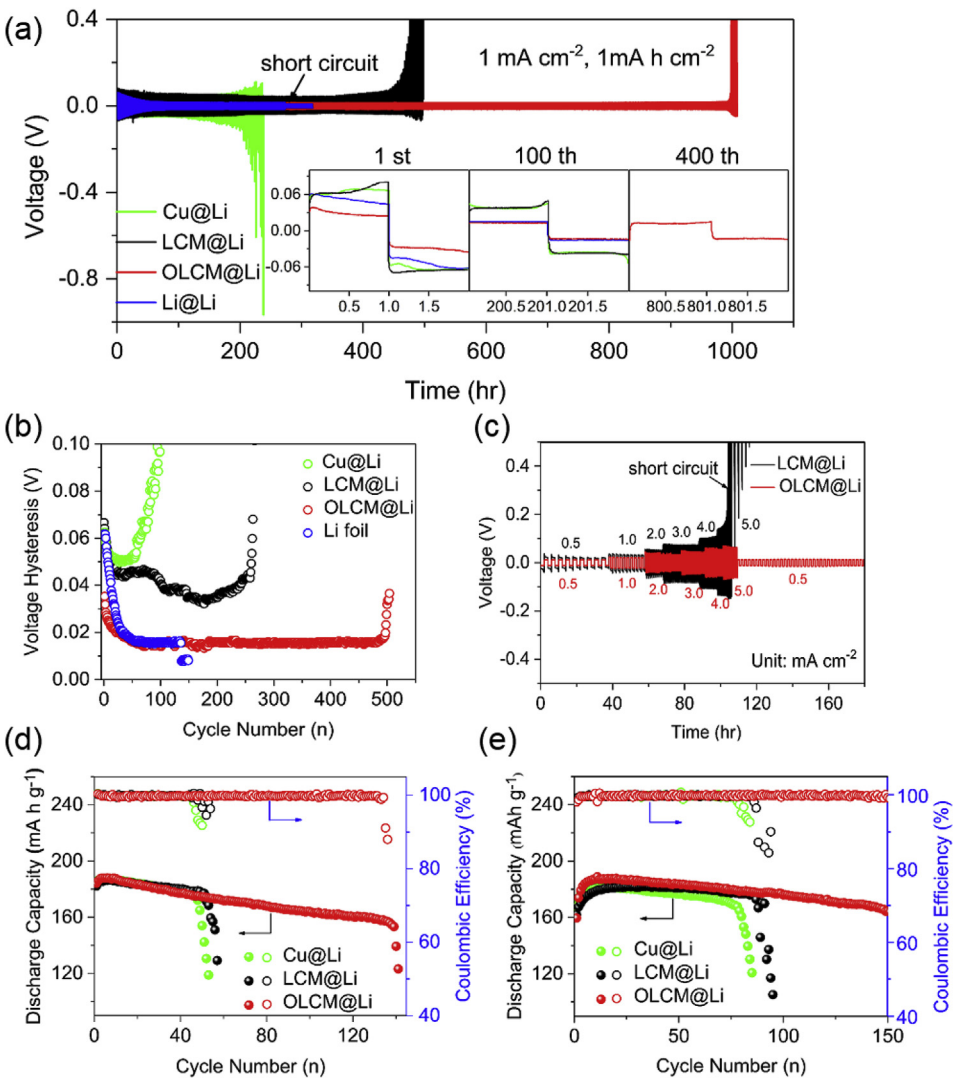

Fig. 4. (a) Voltage profiles of Li metal plating/stripping in four cells (Cu@Li||Li foil, LCM@Li||Li foil, OLCM@Li||Li foil, and Li foil||Li foil) measured at current density of 1 mA cm^{-2} with Li capacity of 1 mA h cm^{-2}. Inset shows Li plating/stripping profiles of the 1st, 100th, and 400th cycles, respectively. (b) The corresponding average voltage hysteresis measured at 1 mA cm^{-2} for 1 mA h cm^{-2}. (c) Rate performance of the LCM@Li||Li foil and OLCM@Li||Li foil cells measured at current densities of 0.5, 1.0, 2.0, 3.0, 4.0 and 5.0 mA cm^{-2} for same Li capacity of 1 mAh cm^{-2}. Cycling performance of the OLCM@Li||NMC811 cells in comparison with the Cu@Li||NMC811 and LCM@Li||NMC811 cells measured at 1.0 C between 2.5 V and 4.5 V, (d) capacity ratio: $C_{NMC811}/C_{Li} = 1.6/6.0$, and (e) Capacity ratio: $C_{NMC811}/C_{Li} = 0.8/6.0$). Note that the actual metallic lithium on the carbon skeleton was much leaner than the nominal loading calculated from the coulometry because some deposited Li would react with the electrolyte to form non-metallic Li compounds.

consumption of the OLCM@Li anode. When we decreased the Li plating to 3 mA h cm^{-2}, the OLCM@Li cell ($C_{NMC811}/C_{Li} = 1.6/3.0$) delivered a similar reversible discharge capacity and cycling stability. After 55 cycles at ~0.8C, the capacity retention still remained at 94% (Fig. S13c, Supporting Information). We thus conjectured that, for the Cu@Li, and LCM@Li anodes, a larger excess Li metal deposition was needed to provide the same cycle performance as the cell containing the OLCM@Li anode. Here we decreased the cathode/anode capacity ratio to $C_{NMC811}/C_{Li} = 0.8/6.0$, the Cu@Li and LCM@Li cells displayed a longer cycle life than before, but still experienced a sudden capacity drop after 80 cycles (Fig. 4e). However, the OLCM@Li anode exhibited a much better performance with reversible discharge capacity staring from 187 mA h g^{-1}, and remained 164 mA h g^{-1} (approximate 88% of the initial reversible capacity) after 150 cycles at 1.0 C (Fig. 4e). This performance was better than NMC811 cells that used bulk Li metal anodes with reversible discharge capacity staring from 192 mA h g^{-1} and remained 152 mA h g^{-1} at 1.0 C (~79% retention) (Fig. S14, Supporting Information), also better than several reported [44,56]. The discharge capacity started fluctuating after 150 cycles, although the cell did not short (Fig. S15, Supporting Information), indicates that more engineering work is needed to further stabilize the cells. The morphology of OLCM@Li didn't change significantly after 10 cycles in full cell compared to the pristine state (after plating), while after 150 cycles, the agglomerated Li particles were clearly seen (Fig. S16, Supporting Information), but the carbon skeleton seems mostly intact. Based on the work published by Niu et al., we believe that in a full battery, cycling at a low current density is more beneficial to the uniform deposition of Li, and hence reducing the lithium consumption and improving the long cycle performance [34]. Other works were also compared with our materials in terms of lithium loading and the cycle performance (Table S2, Supporting Information). The reported studies, listed in Table S2, exclusively used low-voltage (S, $LiFePO_4$) or low-capacity ($LiCoO_2$) cathode materials. The reported OLCM@Li not only allowed for cycling the high-capacity, high voltage NMC811cathode but also provided a higher lithium utilization and more stable cycle performance.

3. Conclusion

In summary, we prepared natural lignin-derived OLCM through electrospinning and surface ozonolysis. Natural lignin is widely available, low cost, and for the first time, used to fabricate the lithiophilic skeleton to host Li metal for nickel-rich layered oxide Li metal batteries. Because of the homogeneously distributed oxygen-containing functional groups, the OLCM offered uniformly distributed Li nucleation sites to guide the uniform Li growth during lithium metal deposition. The lean Li metal anode hosted in the OLCM skeleton exhibited high and stable Coulombic efficiency (>98% over 230 cycles), long cycle life (>1, 000 h), and small voltage hysteresis (<20 mV). The nickel-rich layered oxide batteries, assembled with the lean Li@OLCM composite anode, delivered high initial discharge capacities. Compared with the Cu and LCM hosts,

the OLCM host improved the cycle life of the nickel-rich layered oxide batteries at various C_{NMC811}/C_{Li} capacity ratios due to the decelerated Li consumption. The present study investigated the performance of carbon hosts without the interference of bulk properties using the surface-targeted ozonolysis method. Further advances in the performance of these lightweight, low-cost, flexible, and natural lignin-derived carbon membranes are foreseeable by engineering the carbon crystal structure and cell chemistry.

4. Experimental procedures

4.1. Synthesis of lignin-based carbon membrane (LCM) and oxygen-enriched lignin-based carbon membrane (OLCM)

The LCM was prepared according to the following procedure. 14.1 g lignin (Shandong Longli Biotechnology Co.), 9.4 g phenol, 2.0 g sodium hydroxide, and 29.4 g formaldehyde were mixed in a 250-ml three-neck flask. The mixture was then reacted at 82 °C for 1 h and further reacted at 87 °C for 2 h. After that, 5.5 g polyvinyl alcohol solution was added to adjust the electrospinnability. The resultant solution was electrospun using an electrospinning device (ET-2525H, Ucalery Co.) at high voltages of 16 kV and -1kV. The collected membrane was dried at room temperature and then carbonized at 1000 °C for 2 h in nitrogen atmosphere heating at 5 °C/min. The derived samples were denoted as LCM.

For preparing the OLCM, the carbonized LCM was irradiated for 2 h (1 h for each side) using an ultraviolet/ozone (UV/O_3, PSD UV Ozone System, Novascan, USA) lamp (wavelength: 185 nm) at room temperature and ambient pressure. The distance between the UV lamp and the sample stage was fixed at 20 mm. The flow rate of oxygen was controlled at 0.5 L/min and the released oxygen was converted to ozone to oxidize the samples. After that, all the samples were directly cut into disks (10 mm diameter) as the hosts to accommodate Li metal.

4.2. Electrochemical measurements

To evaluate the electrochemical performance, three types of coin cells (CR2032) were assembled in an Ar-filled glove box using Li foil (the thickness was 0.45 mm, purchased from Jinghong New Energy, China) as counter/reference electrode, Whatman glass fiber as separator, OLCM, LCM and planar Cu as working electrodes, respectively. For electrolyte preparation, 1.0 M lithium bis(trifluoromethanesulfonyl)- imide (LiTFSI) was dissolved into the mixture of 1,3-dioxolane (DOL) and1,2-dimethoxyethane (DME) (1:1 w/w), and then 1 wt% lithium nitrate was added and dispersed completely. About 40 μL electrolyte was added into each coin cell. In order to eliminate impurities and form stable solid electrolyte interphase (SEI) on the surface of OLCM, LCM and Cu, an activation process was conducted. In detail, the cells were firstly cycled between 0 and 1 V (versus Li/Li^+) at a current density of 0.2 mA cm^{-2} for 5 cycles. Then a designated amount of metallic Li (calculated based on the areal capacity) was plated onto these electrodes at a constant current to evaluate the lithium plating behavior, denoted as OLCM@Li, LCM@Li and Cu@Li, respectively. To calculate the Coulombic efficiency (CE), different capacities of metallic Li were plated onto the OLCM, LCM and planar Cu at a constant current density and stripped when charging to 1 V for each cycle. The Coulombic efficiency was calculated based on the charging and discharging capacity. A LANDHE battery system was used for the Coulombic efficiency measurement.

To analyze the long cycle stability, voltage hysteresis and rate performance, the cells were first pre-plated with 6 mA h cm^{-2} Li onto the OLCM and LCM under 0.5 mA cm^{-2} and then plated/stripped at 0.5 mA cm^{-2} for 120 min, at 1 mA cm^{-2} for 60 min, at 2 mA cm^{-2} for 30 min, at 3 mA cm^{-2} for 20 min, at 4 mA cm^{-2} for 15 min and at 5 mA cm^{-2} for 12 min, respectively. For the controlled samples, Cu foil and bare Li foil were employed to replace the OLCM, making cells with the other conditions to be the same.

Full batteries were assembled using $LiNi_{0.8}Mn_{0.1}Co_{0.1}$ (NMC811) as the cathode, Whatman glass fiber as separator, 1.0 M $LiPF_6$ dissolving in the mixture of ethyl carbonate (EC) and dimethyl carbonate (DMC) (1:1 v/v) with 2 wt% vinyl carbonate (VC) as electrolyte, and OLCM@Li, LCM@Li, Cu@Li and pure Li foil as the anodes, respectively. To prepare $LiNi_{0.8}Mn_{0.1}Co_{0.1}$ cathodes, $LiNi_{0.8}Mn_{0.1}Co_{0.1}$ (CAMP/Argonne), carbon black and polyvinylidene difluoride (PVDF) binder (at a mass ratio of 90:5:5) were mixed in *N*-methyl-2-pyrrolidone to form slurry. The slurry was coated onto the Al current collector and the mass loading of the active materials were ~8 mg cm^{-2} (~1.6 mA h cm^{-2}) or ~ 4 mg cm^{-2} (~0.8 mA h cm^{-2}). Galvanostatic discharge/charge measurements were performed on a LANDHE battery testing system with a cutoff potential range of 2.5–4.5 V at room temperature.

4.3. Materials characterization

The morphology of LCM and OLCM before and after Li plating was characterized using scanning electron microscope (FESEM, LEO 1550) and high-resolution transmission electron microscopy (HRTEM, JEOL JEM 2100). To prepare SEM samples, the cells at different stages were disassembled in the Ar-filled glove box and the electrodes were washed with DOL solvent for several times to remove the residual electrolyte. Then, the electrodes were stored in a sealed container with helium balloons and transferred into the vacuum chamber of the SEM without exposure to air. For the TEM samples, the preprocessed electrodes were first immersed in DOL solvent and sonicated for 10 min in a sealed vial. Afterwards, the fully dispersed electrodes were deposited onto the copper grids. After the copper grids were dried in the glove box, they were transferred into the vacuum chamber of the TEM using a specially designed device. The functional groups of LCM and OLCM were quantitatively characterized by X-ray photoelectron spectroscopy (XPS, PHI VersaProbe III) using monochromatic Al K-alpha X-ray source (1486.6 eV). Water contact angle measurements were performed on a FTA 200 contact angle analyzer (First Ten Angstroms, Portsmouth, VA) using a sessile drop technique. Samples were placed on an adjustable platform and ≈5 μL of ultrapure water (Millipore Synergy UV) was placed on the surface using a 3 mL 22 gauge syringe. Raman spectra were collected using a PerkinElmer Raman-Station 400. The specific surface area was measured using automatic physical adsorption/desorption apparatus (ASAP2020, Micromeritics). Synchrotron X-ray diffraction studies were performed at beamline 11−3 at SSRL.

Author contribution

F.L. conceived and led the project. L.T. performed the materials synthesis, performance testing, and characterization. Z.Z. and C.J. assisted in materials synthesis. Z.X. performed the SEM measurements. C.G.K. and X.Z. collected and analyzed the TEM data. C.W. and A.R.E. collected and analyzed the contact angle data. L.T. and F.L. analyzed all data and wrote the manuscript with assistance from all the coauthors.

Conflicts of interest

The authors declare no conflict of interest.

Acknowledgements

The work was supported by Virginia Tech Department of Chemistry Startup Funds, Institute for Critical Technology and Applied Science, and National Science Foundation (Grant No. DMR-1832613.). L.T., C.J. and Z.Z. would like to acknowledge the National Natural Science Foundation of China (No. 31870570, No. 31670599), and the Scientific Research Start-up Funding for Special Professor of Minjiang Scholars. The authors also acknowledge Dr. Xu Feng for his technical assistance with XPS. The XPS work was performed in the Surface Analysis Laboratory in Department of Chemistry at Virginia Tech, which is supported by the National Science Foundation under Grant No. CHE-1531834. The authors would

further like to acknowledge Dr. Yiming Feng for his assistance in Raman data. L.T. thanks D. Kautz for the technical assistance in the electrical measurements. Use of the Stanford Synchrotron Radiation Lightsource, SLAC National Accelerator Laboratory, is supported by the U.S. Department of Energy, Office of Science, Office of Basic Energy Sciences under Contract No. DE-AC02-76SF00515. The NMC811 powder was produced at the U.S. Department of Energy's (DOE) CAMP (Cell Analysis, Modeling and Prototyping) Facility, Argonne National Laboratory. The CAMP Facility is fully supported by the DOE Vehicle Technologies Program (VTP) within the core funding of the Applied Battery Research (ABR) for Transportation Program.

Appendix A. Supplementary data

Supplementary data to this article can be found online at https://doi.org/10.1016/j.ensm.2019.08.027.

References

[1] J. Liu, Z. Bao, Y. Cui, E.J. Dufek, J.B. Goodenough, P. Khalifah, Q. Li, B.Y. Liaw, P. Liu, A. Manthiram, Y.S. Meng, V.R. Subramanian, M.F. Toney, V.V. Viswanathan, M.S. Whittingham, J. Xiao, W. Xu, J. Yang, X.Q. Yang, J.G. Zhang, Pathways for practical high-energy long-cycling lithium metal batteries, Nat. Energy 4 (2019) 180–186.
[2] D. Lin, Y. Liu, Y. Cui, Reviving the lithium metal anode for high-energy batteries, Nat. Nanotechnol. 12 (2017) 194–206.
[3] P. Albertus, S. Babinec, S. Litzelman, A. Newman, Status and challenges in enabling the lithium metal electrode for high-energy and low-cost rechargeable batteries, Nat. Energy 3 (2018) 16–21.
[4] S. Nanda, A. Gupta, A. Manthiram, A lithium – sulfur cell based on reversible lithium deposition from a Li 2 S cathode host onto a hostless- anode substrate, Adv. Energy Mater. 8 (2018) 1801556.
[5] J. Betz, J. Brinkmann, R. Nölle, C. Lürenbaum, M. Kolek, M.C. Stan, M. Winter, T. Placke, Cross talk between transition metal cathode and Li metal Anode : unraveling its influence on the deposition/dissolution behavior and morphology of lithium, Adv. Energy Mater. (2019) 1900574.
[6] W. Kwak, S. Park, H. Jung, Y. Sun, Optimized concentration of redox mediator and surface protection of Li metal for maintenance of high energy efficiency in Li – O 2 batteries, Adv. Energy Mater. 8 (2018) 1702258.
[7] R.V. Salvatierra, G.A. López-Silva, A.S. Jalilov, J. Yoon, G. Wu, A.L. Tsai, J.M. Tour, Suppressing Li metal dendrites through a solid Li-ion backup layer, Adv. Mater. 30 (2018) 1803869.
[8] J. Lee, M. Shin, D. Hong, S. Park, Efficient Li-Ion-Conductive layer for the realization of highly stable high-voltage and high-capacity lithium metal batteries, Adv. Energy Mater. 9 (2019) 1803722.
[9] S. Jurng, Z.L. Brown, J. Kim, B.L. Lucht, Effect of electrolyte on the nanostructure of the solid electrolyte interphase (SEI) and performance of lithium metal anodes, Energy Environ. Sci. 11 (2018) 2600–2608.
[10] J. Zheng, M.H. Engelhard, D. Mei, S. Jiao, B.J. Polzin, J.G. Zhang, W. Xu, Electrolyte additive enabled fast charging and stable cycling lithium metal batteries, Nat. Energy 2 (2017) 17012.
[11] N.D. Trinh, D. Lepage, D. Aymé-Perrot, A. Badia, M. Dollé, D. Rochefort, An artificial lithium protective layer that enables the use of acetonitrile-based electrolytes in lithium metal batteries, Angew. Chem. Int. Ed. 57 (2018) 5072–5075.
[12] M.D. Tikekar, S. Choudhury, Z. Tu, L.A. Archer, For stable lithium-metal batteries, Nat. Energy 1 (2016) 16114.
[13] J. Lau, R.H. Deblock, D.M. Butts, D.S. Ashby, C.S. Choi, B.S. Dunn, Sulfide solid electrolytes for lithium battery applications, Adv. Energy Mater. 8 (2018) 1800933.
[14] V. Viswanathan, Machine learning enabled computational screening of inorganic solid electrolytes for suppression of dendrite formation in lithium metal anodes, ACS Cent. Sci. 4 (2018) 996–1006.
[15] J. Alvarado, M.A. Schroeder, T.P. Pollard, X. Wang, J.Z. Lee, M. Zhang, T. Wynn, M. Ding, O. Borodin, Y.S. Meng, K. Xu, Bisalt ether electrolytes: a pathway towards lithium metal batteries with Ni-rich cathodes, Energy Environ. Sci. 12 (2019) 780–794.
[16] M.S. Kim, J.H. Ryu, Deepika, Y.R. Lim, I.W. Nah, K.R. Lee, L.A. Archer, W. Il Cho, Langmuir–Blodgett artificial solid-electrolyte interphases for practical lithium metal batteries, Nat. Energy 3 (2018) 889–898.
[17] S. Jin, Y. Jiang, H. Ji, Y. Yu, Advanced 3D current collectors for lithium-based batteries, Adv. Mater. 30 (2018) 1802014.
[18] Y. An, H. Fei, G. Zeng, X. Xu, L. Ci, B. Xi, S. Xiong, J. Feng, Y. Qian, Vacuum distillation derived 3D porous current collector for stable lithium–metal batteries, Nano Energy 47 (2018) 503–511.
[19] C.P. Yang, Y.X. Yin, S.F. Zhang, N.W. Li, Y.G. Guo, Accommodating lithium into 3D current collectors with a submicron skeleton towards long-life lithium metal anodes, Nat. Commun. 6 (2015) 8058.
[20] Q. Yun, Y.-B. He, W. Lv, Y. Zhao, B. Li, F. Kang, Q.-H. Yang, Chemical dealloying derived 3D porous current collector for Li metal anodes, Adv. Mater. 28 (2016) 6932–6939.
[21] X. Yue, W. Wang, Q. Wang, J. Meng, Z. Zhang, CoO nano fiber decorated nickel foams as lithium dendrite suppressing host skeletons for high energy lithium metal batteries, Energy Storage Mater. 14 (2018) 335–344.
[22] Q. Li, S. Zhu, Y. Lu, 3D porous Cu current collector/Li-metal composite anode for stable lithium-metal batteries, Adv. Funct. Mater. 27 (2017) 1606422.
[23] H. Zhao, D. Lei, Y.B. He, Y. Yuan, Q. Yun, B. Ni, W. Lv, B. Li, Q.H. Yang, F. Kang, J. Lu, Compact 3D copper with uniform porous structure derived by electrochemical dealloying as dendrite-free lithium metal anode current collector, Adv. Energy Mater. 8 (2018) 1800266.
[24] H. Ye, S. Xin, Y.X. Yin, Y.G. Guo, Advanced porous carbon materials for high-efficient lithium metal anodes, Adv. Energy Mater. 7 (2017) 1700530.
[25] R. Zhang, X.R. Chen, X. Chen, X.B. Cheng, X.Q. Zhang, C. Yan, Q. Zhang, Lithiophilic sites in doped graphene guide uniform lithium nucleation for dendrite-free lithium metal anodes, Angew. Chem. Int. Ed. 56 (2017) 7764.
[26] R. Zhang, N.W. Li, X.B. Cheng, Y.X. Yin, Q. Zhang, Y.G. Guo, Advanced micro/nanostructures for lithium metal anodes, Adv. Sci. 4 (2017) 1600445.
[27] S. Liu, A. Wang, Q. Li, J. Wu, K. Chiou, J. Huang, J. Luo, Crumpled graphene balls stabilized dendrite-free lithium metal anodes, Joule 2 (2018) 184.
[28] T.T. Zuo, X.W. Wu, C.P. Yang, Y.X. Yin, H. Ye, N.W. Li, Y.G. Guo, Graphitized carbon fibers as multifunctional 3D current collectors for high areal capacity Li anodes, Adv. Mater. 29 (2017) 1700389.
[29] S. Jin, Z. Sun, Y. Guo, Z. Qi, C. Guo, X. Kong, Y. Zhu, H. Ji, High areal capacity and lithium utilization in anodes made of covalently connected graphite microtubes, Adv. Mater. 29 (2017) 1700783.
[30] J. Xie, J. Ye, F. Pan, X. Sun, K. Ni, H. Yuan, X. Wang, N. Shu, C. Chen, Y. Zhu, Incorporating flexibility into stiffness: self-grown carbon nanotubes in melamine sponges enable a lithium-metal-anode capacity of 15 mAh cm^{-2} cyclable at 15 mA cm^{-2}, Adv. Mater. 31 (2019) 1805654.
[31] H. Wang, D. Lin, J. Xie, Y. Liu, H. Chen, Y. Li, J. Xu, G. Zhou, Z. Zhang, A. Pei, Y. Zhu, K. Liu, K. Wang, Y. Cui, An interconnected channel-like framework as host for lithium metal composite anodes, Adv. Energy Mater. 9 (2019) 1802720.
[32] M.S. Silberberg, P. Amateis, Chemistry: the Molecular Nature of Matter and Change, Mosby, St. Louis, Missouri, USA, 1996.
[33] J. Cui, S. Yao, M. Ihsan-Ul-Haq, J. Wu, J.K. Kim, Correlation between Li plating behavior and surface characteristics of carbon matrix toward stable Li metal anodes, Adv. Energy Mater. 9 (2019) 1802777.
[34] C. Niu, H. Pan, W. Xu, J. Xiao, J.G. Zhang, L. Luo, C. Wang, D. Mei, J. Meng, X. Wang, Z. Liu, L. Mai, J. Liu, Self-smoothing anode for achieving high-energy lithium metal batteries under realistic conditions, Nat. Nanotechnol. 14 (2019) 594–601.
[35] Y. Zhang, C. Wang, G. Pastel, Y. Kuang, H. Xie, Y. Li, B. Liu, W. Luo, C. Chen, L. Hu, 3D wettable framework for dendrite-free alkali metal anodes, Adv. Energy Mater. 8 (2018) 1800635.
[36] H. Qiu, T. Tang, M. Asif, W. Li, T. Zhang, Y. Hou, Stable lithium metal anode enabled by lithium metal partial alloying, Nano Energy 65 (2019) 103989.
[37] L. Liu, Y.X. Yin, J.Y. Li, S.H. Wang, Y.G. Guo, L.J. Wan, Uniform lithium nucleation/growth induced by lightweight nitrogen-doped graphitic carbon foams for high-performance lithium metal anodes, Adv. Mater. 30 (2018) 1706216.
[38] F. Liang, L. Lin, Z. Feng, C. Chu, J. Pan, J. Yang, Y. Qian, Spatial separation of lithiophilic surface and superior conductivity for advanced Li metal anode: the case of acetylene black and N-doped carbon spheres, J. Mater. Chem. A. 7 (2019) 8765–8770.
[39] R. Zhang, S. Wen, N. Wang, K. Qin, E. Liu, C. Shi, N. Zhao, N-doped graphene modified 3D porous Cu current collector toward microscale homogeneous Li deposition for Li metal anodes, Adv. Energy Mater. 8 (2018) 1800914.
[40] X. Chen, X.R. Chen, T.Z. Hou, B.Q. Li, X.B. Cheng, R. Zhang, Q. Zhang, Lithiophilicity chemistry of heteroatom-doped carbon to guide uniform lithium nucleation in lithium metal anodes, Sci. Adv. 5 (2019) aau7728.
[41] G. Huang, J. Han, F. Zhang, Z. Wang, H. Kashani, K. Watanabe, M. Chen, Lithiophilic 3D nanoporous nitrogen-doped graphene for dendrite-free and ultrahigh-rate lithium-metal anodes, Adv. Mater. 31 (2019) 1805334.
[42] K. Liu, Z. Li, M. Wei, Oxygen-rich carbon nanotube networks for enhanced lithium metal anode, Energy Storage Mater. 15 (2018) 308–314.
[43] Z. Xu, M. Rahman, L. Mu, Y. Liu, Chemomechanical behaviors of layered cathode, J. Mater. Chem. A. 6 (2018) 21859–21884.
[44] J.D. Steiner, L. Mu, J. Walsh, M.M. Rahman, B. Zydlewski, F.M. Michel, H.L. Xin, D. Nordlund, F. Lin, Accelerated evolution of surface chemistry determined by temperature and cycling history in nickel-rich layered cathode materials, ACS Appl. Mater. Interfaces 10 (2018) 23842–23850.
[45] C. Tian, F. Lin, Electrochemical characteristics of layered transition metal oxide cathode materials for lithium ion batteries: surface, bulk behavior, and thermal properties, Acc. Chem. Res. 51 (2018) 89–96.
[46] W. Liu, P. Oh, X. Liu, M. Lee, W. Cho, S. Chae, Y. Kim, J. Cho, Nickel-rich layered lithium transition-metal oxide for high-energy lithium-ion batteries, Angew. Chem. Int. Ed. 54 (2015) 4440–4457.
[47] F. Lin, I.M. Markus, D. Nordlund, T. Weng, M.D. Asta, H.L. Xin, M.M. Doeff, Surface reconstruction and chemical evolution of stoichiometric layered cathode materials for lithium-ion batteries, Nat. Commun. 5 (2014) 3529.
[48] F. Lin, D. Nordlund, Y. Li, M.K. Quan, L. Cheng, T. Weng, Y. Liu, H.L. Xin, M.M. Doe, Metal segregation in hierarchically structured cathode materials for high-energy lithium batteries, Nat. Energy 1 (2016) 15004.
[49] L. Mu, Q. Yuan, C. Tian, C. Wei, K. Zhang, J. Liu, M.M. Doeff, Y. Liu, F. Lin, Propagation topography of redox phase transformations in heterogeneous layered oxide cathode materials, Nat. Commun. 9 (2018) 2810.

[50] G. Yang, Y. Li, Y. Tong, J. Qiu, S. Liu, S. Zhang, Z. Guan, B. Xu, Z. Wang, L. Chen, Lithium plating and stripping on carbon nanotube sponge, Nano Lett. 19 (2018) 494–499.
[51] Y. Huang, L. Peng, Y. Liu, G. Zhao, J.Y. Chen, G. Yu, Biobased nano porous active carbon fibers for high-performance supercapacitors, ACS Appl. Mater. Interfaces 8 (2016) 15205–15215.
[52] S. Homaeigohar, T. Strunskus, J. Strobel, L. Kienle, M. Elbahri, A flexible oxygenated carbographite nanofilamentous buckypaper as an amphiphilic membrane, Adv. Mater. Interfaces 5 (2018) 1800001.
[53] L. Liu, Y. Yin, J. Li, L. Liu, Y. Yin, J. Li, N. Li, X. Zeng, H. Ye, Y. Guo, Free-standing hollow carbon fibers as high- capacity containers for stable lithium metal anodes, Joule 1 (2017) 563–575.
[54] D.J. Kautz, L. Tao, L. Mu, D. Nordlund, X. Feng, Z. Zheng, F. Lin, Understanding the critical chemistry to inhibit lithium consumption in lean lithium metal composite anodes, J. Mater. Chem. 6 (2018) 16003–16011.
[55] X. Ren, L. Zou, S. Jiao, D. Mei, M.H. Engelhard, Q. Li, H. Lee, C. Niu, B.D. Adams, C. Wang, J. Liu, J.G. Zhang, W. Xu, High-concentration ether electrolytes for stable high-voltage lithium metal batteries, ACS Energy Lett. 4 (2019) 896–902.
[56] S. Gao, Y. Cheng, M. Shirpour, S. Gao, Y.-T. Cheng, M. Shirpour, Effects of cobalt deficiency on nickel-rich layered $LiNi_{0.8}Co_{0.1}Mn_{0.1}O_2$ positive electrode matrials for lithium-ion batteries, ACS Appl. Mater. Interfaces 11 (2019) 982–989.